

SUPPLEMENTARY MATERIAL TO:

Limebeer and Graham. S Afr J Sci. 2026;122(3/4), Art. #22766.

<https://doi.org/10.17159/sajs.2026/22766>

HOW TO CITE:

Limebeer DJN, Graham M. Biomechanics of the slingshot spider and its three-dimensional web [supplementary material]. S Afr J Sci. 2026;122(3/4), Art. #22766.

<https://doi.org/10.17159/sajs.2026/22766/suppl>

Appendices (A–I)

A. Web construction

The web of an orb spider is a special case of a tensegrity framework—these frameworks are of great interest to engineers, scientists and mathematicians alike^{1,2,3,4}.

Given a fixed set of anchor points, the first step in the web construction is determining the location of the radial thread junction point. As the reader will appreciate, the location of this point will determine the radial thread stiffnesses as well as the web's dynamic response. As with many civil engineering projects, the aim is to minimise material usage whilst also avoiding long structural members. To that end, we propose a performance criterion for the web radial thread meeting point that minimizes thread material usage, while also discouraging the use of damage-prone long radial threads. Suppose the web's N anchor points are given by \mathbf{p}_n for $1 \leq n \leq N$, with their unknown junction point given by \mathbf{x}_s . The material usage criterion, which is a measure of the length-squared usage of all the radial threads is given by

$$\mathcal{J} = \frac{1}{2} \sum_{n=1}^N \|\mathbf{p}_n - \mathbf{x}_s\|_2^2; \quad (\text{A.1})$$

the factor of a half is a convenient scaling constant. We will use the outcome of the minimization of \mathcal{J} to find the thread rest lengths as well as their spring constants. It is immediate that

$$\nabla \mathcal{J} = \left[Nx_s - \sum_{n=1}^N x_n; Ny_s - \sum_{n=1}^N y_n; Nz_s - \sum_{n=1}^N z_n \right];$$

with the components of \mathbf{x}_s and \mathbf{p}_n given by $[x_s; y_s; z_s]$ and $[x_n; y_n; z_n]$ respectively. A thread-length stationary point occurs when $\nabla \mathcal{J} = \mathbf{0}$, which occurs when \mathbf{x}_s is at the geometric centre of the set of anchor points:

$$\mathbf{x}_s^* = \frac{1}{N} \sum_{n=1}^N x_n; \quad \mathbf{y}_s^* = \frac{1}{N} \sum_{n=1}^N y_n; \quad \mathbf{z}_s^* = \frac{1}{N} \sum_{n=1}^N z_n; \quad (\text{A.2})$$

$\mathbf{x}_s^* = [x_s^*; y_s^*; z_s^*]$. Since the Hessian of \mathcal{J} is positive definite, (A.2) constitutes a minimum that is both global and unique⁵.

Once the minimum \mathbf{x}_s^* has been found, the N radial thread rest lengths will be given by $\|\mathbf{x}_s^* - \mathbf{p}_n\|_2$, with their associated elastic spring forces described by

$$\mathbf{f}_n = -k_n^r \max(\|\mathbf{x}_s - \mathbf{p}_n\|_2 - \|\mathbf{x}_s^* - \mathbf{p}_n\|_2, 0) \frac{\mathbf{x}_s - \mathbf{p}_n}{\|\mathbf{x}_s - \mathbf{p}_n\|_2}, \quad (\text{A.3})$$

since the web fibres cannot produce compressive forces. The various spring constants are given by

$$k_n^r = \frac{AE_r}{\|\mathbf{p}_n - \mathbf{x}_s^*\|_2}; \quad (\text{A.4})$$

A is the cross sectional area of the web fibres and E_r is their Young's modulus. This is a standard relationship between an intrinsic material property (Young's Modulus) and stiffness, which is depended on the size and shape of a cylinder. When the thread operates elastically under tension, that is $\|\mathbf{x}_s - \mathbf{p}_n\|_2 \geq \|\mathbf{x}_s^* - \mathbf{p}_n\|_2$, (A.3) takes the simpler form

$$\mathbf{f}_n = -k_n^r (\Delta \mathbf{x}_s - \mathbf{p}_n). \quad (\text{A.5})$$

Field measurements have shown that the web's stiff radial threads are pre-tensioned in their equilibrium configuration, and that they structurally dominate the web⁶. The rest lengths of the four thread partitions surrounding $\mathbf{p}_0(n, m)$ are given by $\|\mathbf{p}_0(n, m) - \mathbf{p}_0(n \pm 1, m \pm 1)\|_2$, with the stiffnesses of the radial thread partitions given by

$$k_{n, m \pm 1}^r = \frac{AE_r}{\|\mathbf{p}_0(n, m \pm 1) - \mathbf{p}_0(n, m)\|_2}, \quad 1 \leq m \leq M \quad (\text{A.6})$$

for every partition along the n^{th} radial thread, with $\mathbf{p}_0(n, 0) = \mathbf{x}_s^*$ and $\mathbf{p}_0(n, M + 1) = \mathbf{p}_n$. The stiffnesses of the capture threads between $\mathbf{p}_0(n, m)$ and $\mathbf{p}_0(n \pm 1, m)$ are given by

$$k_{n \pm 1, m}^c = \frac{AE_c}{\|\mathbf{p}_0(n \pm 1, m) - \mathbf{p}_0(n, m)\|_2}, \quad 1 \leq n \leq N \quad (\text{A.7})$$

along the m^{th} capture thread. The point $\mathbf{p}_0(0, m)$ wraps around to $\mathbf{p}_0(N, m)$, and $\mathbf{p}_0(N + 1, m)$ wraps around to $\mathbf{p}_0(1, m)$.

In order to make the web operational, the anchor points of the web are now moved outwards putting the web under tension⁷. In our case this will be achieved by increasing \mathcal{A} by 1.0%. The pre-stressed force balance equation for the nodes on the $m = M$ outer ring is given by

$$\begin{aligned} 0 = & +k_{n, M+1}^r (\Delta \mathbf{p}_n - \Delta \mathbf{p}(n, M)) \\ & +k_{n, M-1}^r (\Delta \mathbf{p}(n, M-1) - \Delta \mathbf{p}(n, M)) \\ & +k_{n-1, M}^c (\Delta \mathbf{p}(n-1, M) - \Delta \mathbf{p}(n, M)) \\ & +k_{n+1, M}^c (\Delta \mathbf{p}(n+1, M) - \Delta \mathbf{p}(n, M)) \end{aligned} \quad (\text{A.8})$$

for $1 \leq n \leq N$. The pre-tensioning outward movements of the anchor points are denoted $\Delta \mathbf{p}_n$, while $\Delta \mathbf{p}(n, m)$ represent departures from their relaxed rest positions $\mathbf{p}_0(n, m)$. The force balance on the web's $m = 1$ inner ring are given by another n algebraic equations

$$\begin{aligned} 0 = & +k_{n, 0}^r (\Delta \mathbf{x}_s - \Delta \mathbf{p}(n, 1)) \\ & +k_{n, 2}^r (\Delta \mathbf{p}(n, 2) - \Delta \mathbf{p}(n, 1)) \\ & +k_{n-1, 1}^c (\Delta \mathbf{p}(n-1, 1) - \Delta \mathbf{p}(n, 1)) \\ & +k_{n+1, 1}^c (\Delta \mathbf{p}(n+1, 1) - \Delta \mathbf{p}(n, 1)), \end{aligned} \quad (\text{A.9})$$

for $1 \leq n \leq N$; $\Delta \mathbf{x}_s$ represents the movement of \mathbf{x}_s from \mathbf{x}_s^* due to web tensioning. The force balance equations on $N \times (M - 2)$ interior points are given by

$$\begin{aligned} 0 = & +k_{n, m+1}^r (\Delta \mathbf{p}(n, m+1) - \Delta \mathbf{p}(n, m)) \\ & +k_{n, m-1}^r (\Delta \mathbf{p}(n, m-1) - \Delta \mathbf{p}(n, m)) \\ & +k_{n-1, m}^c (\Delta \mathbf{p}(n-1, m) - \Delta \mathbf{p}(n, m)) \\ & +k_{n+1, m}^c (\Delta \mathbf{p}(n+1, m) - \Delta \mathbf{p}(n, m)), \end{aligned} \quad (\text{A.10})$$

for $1 \leq n \leq N$; $2 \leq m \leq M - 1$. As with (A.8), a "wrap around" must be applied when either n or m fall out of their respective ranges. The force acting on the spider is

$$\mathbf{F}_s = \sum_{n=1}^N k_{n, 0}^r (\Delta \mathbf{p}(n, 1) - \Delta \mathbf{x}_s). \quad (\text{A.11})$$

Since each of the equations in (A.8), (A.9), (A.10) and (A.11) are vector equations in \mathbb{R}^3 , a total of $(N \times M + 1) \times 3$ equations must be solved. Following the solution of these equations, the web is again in equilibrium, but this time pre-stressed.

Finally, we can obtain the dynamic equations of the undamped web by adding 6 differential equations associated with the spider's dynamics (Newton's second law in three dimensions) to the algebraic web force equations:

$$m_s \ddot{\mathbf{x}}_s = \mathbf{F}_s. \quad (\text{A.12})$$

When (A.12) is combined with the $(N \times M + 1) \times 3$ force-balance equations, the web dynamics are described by a differential-algebraic equation system comprising $(N \times M) \times 3$ algebraic equations and 6 differential equations. Since the system in this form is conservative, ever-persistent oscillations with a single undamped resonant frequency are to be expected.

B. Aerodynamics of a sphere

An incompressible viscous fluid with aerodynamic flow is described by the Navier-Stokes equations

$$\frac{\partial \mathbf{v}}{\partial t} + (\mathbf{v} \cdot \nabla) \mathbf{v} = -\frac{1}{\rho} \nabla p + \nu \nabla^2 \mathbf{v} \quad \text{and} \quad \nabla \cdot \mathbf{v} = 0 \quad (\text{B.1})$$

in which \mathbf{v} is the velocity of the fluid, p is the pressure distribution, $\nu = \eta/\rho$ is the kinematic viscosity, η is the dynamic viscosity and ρ is the fluid density. The small size of the spider $\approx 1 \text{ mm}$ in diameter, moving at velocities of $\leq 10 \text{ m s}^{-1}$, implies a range of Reynolds number (Re_e) between 0 and a few 100s. In this range the flow around the spider's body, considered here to be spherical, will be laminar and well below the drag crisis irrespective of disruptions to the flow caused by hairs, legs and web lines. The Reynolds number range for the web lines is much lower, $\ll 1$, because of their much smaller diameters. Stokes⁸ solved (B.1) for very low Reynolds number flows (applicable only when $Re_e \ll 1$,⁹) when the quadratic convection acceleration term can be ignored, and found that the force acting on an oscillating sphere of radius a is given by

$$\begin{aligned} \mathbf{F}_D &= 6\pi\eta a \left(1 + \frac{a}{\delta}\right) \mathbf{v} + 3\pi a^2 \rho \delta \left(1 + \frac{2a}{9\delta}\right) \dot{\mathbf{v}} \\ &= 6\pi\eta a \left(1 + \frac{a}{\delta}\right) \mathbf{v} + \left\{ \frac{3\rho}{4} (4\pi a^2 \delta) + \underbrace{\left(\frac{4}{3}\pi a^3\right) \frac{\rho}{2}}_{m_a} \right\} \dot{\mathbf{v}}, \end{aligned} \quad (\text{B.2})$$

where $\delta = \sqrt{\frac{2\nu}{\omega}}$ is the thickness of the boundary layer surrounding the sphere, while ω is the angular frequency of the motion. The first term on the right-hand side of (B.2) is the laminar friction drag coefficient, the second term represents $3/4$ of the mass of the fluid in the spherical shell boundary layer surrounding the sphere, while the third term is one half of the mass of the fluid displaced by the sphere; the fluid "added-mass" m_a .

Stokes' result⁸ was extended in subsequent theoretical work^{10,11,12}, to the three-term Basset–Boussinesq–Oseen (BBO) equation

$$\mathbf{F}_D = 6\pi a \eta \mathbf{v} + \frac{1}{2} \left(\frac{4}{3}\pi a^3 \rho\right) \dot{\mathbf{v}} + 6a^2 \sqrt{\pi \eta \rho} \int_{t_0}^t \frac{\dot{\mathbf{v}}(\tau)}{\sqrt{t-\tau}} d\tau. \quad (\text{B.3})$$

In this equation the first term on the right-hand side is the steady-state viscous drag (the Stokes drag). The second term is the resistance to accelerations (the added-mass term), while the third term represents the acceleration history (the Basset memory term), which recognises the influences of the wake which can be strong in a reversing flow.

Equation (B.3) was modified to include a quadratic velocity drag term extending its range of validity to higher Reynolds numbers as the convective acceleration becomes increasingly important¹³:

$$\mathbf{F}_D = \frac{1}{2} C_D \pi a^2 \rho |\mathbf{v}| \mathbf{v} + C_A \left(\frac{4}{3}\pi a^3 \rho\right) \dot{\mathbf{v}} + C_H a^2 \sqrt{\pi \rho \eta} \int_{t_0}^t \frac{\dot{\mathbf{v}}(\tau)}{\sqrt{t-\tau}} d\tau \quad (\text{B.4})$$

in which C_D is the steady-state drag coefficient, C_A is the added-mass coefficient, and C_H is the history coefficient. Without the history term this equation is the same as the widely used Morison equation¹⁴ for high Reynolds number time varying flows. The $|\mathbf{v}| \mathbf{v}$ form of the quadratic term ensures that this term opposes the body motion in reversing flows.

In the work presented here, we will use (B.4) in which

$$C_D = \frac{24}{Re_e} + \frac{2.6 \left(\frac{Re_e}{5.0}\right)}{1 + \left(\frac{Re_e}{5.0}\right)^{1.52}} + \frac{0.411 \left(\frac{Re_e}{2.63 \times 10^5}\right)^{-7.94}}{1 + \left(\frac{Re_e}{2.63 \times 10^5}\right)^{-8.00}} + \frac{0.25 \left(\frac{Re_e}{10^6}\right)}{1 + \left(\frac{Re_e}{10^6}\right)}, \quad (\text{B.5})$$

with the added-mass and history terms neglected. A calculation based on Section 4 of¹³, provided in Appendix H, is used to justify the neglect of both terms. The steady-state drag coefficient C_D was found by curve fitting to experimental data^{15,16}; see Figure B.1. At $Re_e < 2$, (B.5) is dominated

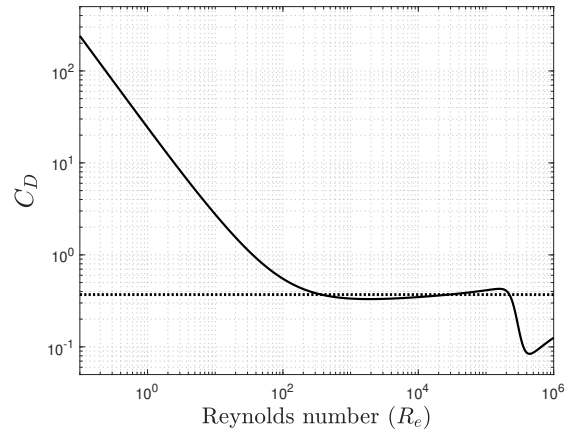


Figure B.1: Drag coefficient for a smooth sphere as predicted by (B.5). The drag crisis is seen to occur at $Re_e \approx 3.0 \times 10^5$.

by the creeping flow term $\frac{24}{Re_e}$. At higher Reynolds numbers, (B.5) plateaus at $C_D \approx 0.37$ over a wide range, well exceeding the highest Reynolds numbers which can occur in the current study and well below the drag crisis. Note that (B.5) is unbounded in the $\lim_{Re_e \rightarrow 0}$. In simulations, we restrict the Reynolds number to the range $0.1 \leq Re_e \leq 10^4$, which is well within the domain of validity of (B.5).

C. Aerodynamics of a cylinder

Stokes⁸ also derived an expression for the viscous damping force on an infinitely-long cylinder vibrating rectilinearly normal to its length with infinitesimal amplitude and $Re \ll 1$. This solution fails for steady flow and¹⁷ showed that the Oseen form of the Navier-Stokes equations¹⁸, is required to derive the drag force which per unit length for an infinite cylinder is given by

$$F_d = 4\pi\eta\epsilon v \quad \text{where} \quad \epsilon = \frac{1}{\frac{1}{2} - \gamma - \log\left(\frac{Re}{8}\right)}, \quad (\text{C.1})$$

where $\gamma = 0.5772$ is the Euler-Mascheroni constant; $Re = 2av/\nu$, a is the radius of the cylinder. A refinement came from Kaplun¹⁹, where the cylinder drag per unit length was found to be

$$F_d = -4\pi\eta v \epsilon (1 - 0.87\epsilon^2). \quad (\text{C.2})$$

It is shown in²⁰ that a slightly better fit to measured data can be obtained by replacing the 0.87 term with $0.61685 = (\pi/4)^2$. In another refinement, the empirical formula

$$C_D = 9.689Re^{-0.78}(1 + 0.147Re^{0.82}) \quad (\text{C.3})$$

for the drag coefficient is given for $0 \leq Re \leq 5$ ²¹. Lamb's original result and the subsequent improvements are shown in Figure C.1. Due to the extremely small diameter of the

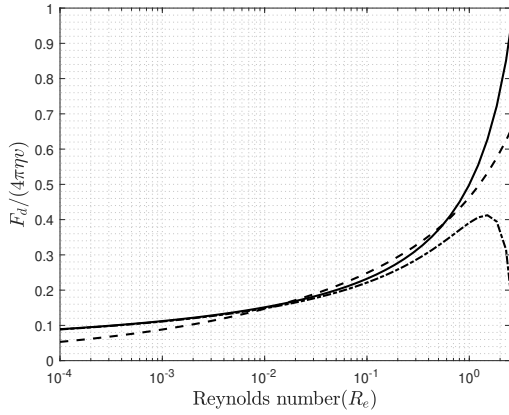


Figure C.1: Drag force on a long cylinder at low Reynolds number. The solid curve corresponds to (C.1), the dot-dash corresponds to (C.2), while the dashed curve comes from (C.3).

web fibres, the Reynolds number for the web fibres is $Re < 1$ making an “infinite aspect ratio” assumption appropriate. The flow conditions along a fibre vary on a length-dependent scale making local sectional flow analysis applicable. Since the ratio of the amplitude of the motion to the diameter of the web fibres is $\mathcal{O}(10^3)$, the small amplitude assumption is problematic. The acceleration terms in the Navier-Stokes equations are of the order

$$(\mathbf{v} \cdot \nabla)\mathbf{v} \sim \frac{A^2}{L} \quad \text{while} \quad \frac{\partial \mathbf{v}}{\partial t} \sim \frac{A}{T}$$

in which A is the amplitude of the velocity oscillation, L is a characteristic length, and T is the period of the oscillation. A characteristic amplitude parameter for oscillatory flows is the Keulegan–Carpenter number, K_c , defined as the ratio of these terms, so that $K_c \sim \frac{AT}{L}$. For sinusoidal motions of the form $x_0 \sin \omega t$, $A \sim x_0 \omega$, $T = \frac{2\pi}{\omega}$, and $L = a$, so that

$$K_c = \frac{2\pi x_0 \omega}{a}, \quad (\text{C.4})$$

where a is the cylinder radius and x_0 is the amplitude of the displacement oscillations. Since $K_c \gg 1$ being in the order of tens of thousands for the motion of the web fibres, the convective acceleration term in the Navier-Stokes equations cannot be neglected, which puts the utility of Stokes' solution (based on Bessel functions) to the cylinder drag problem⁸ in jeopardy for our application. At these large K_c values the added-mass term is much smaller than the drag term and quasi-steady theory for the forces induced becomes accurate throughout the oscillation cycle at all Reynolds numbers; see²² for an example at a higher Reynolds number. To facilitate a simple analysis for a web fibre in large-amplitude unsteady motion, a direct extension of the steady-state formula (C.1), will be used together with a quasi-steady assumption. That is, the instantaneous forces on a fibre in unsteady motion are assumed to be those corresponding to steady motion at the same instantaneous velocity. While Re changes with time, its past history is deemed unimportant. In the range $0 < Re \leq 1$, there is little to choose between (C.1), (C.2) and (C.3), with (C.3) providing an extension to the $0 < Re \leq 5$ range. In simulations we restrict the Reynolds number to $Re \geq 1.0^{-4}$.

D. Drag on the radial lines

We suppose in Figure D.1 that the radial threads behave like pendulums rotating about their anchor points with two angular degrees of freedom. The spider is at point \mathbf{x}_s , with the anchor point for the n^{th} radial thread at \mathbf{p}_n , which is absolutely stationary. The n^{th} radial thread has length $l_n = \|\mathbf{x}_s - \mathbf{p}_n\|_2$. The velocity of the spider can be described by

$$\mathbf{v}_s = \dot{\mathbf{l}}_n + \boldsymbol{\omega}_n \times \mathbf{l}_n, \quad (\text{D.1})$$

where the $\dot{\mathbf{l}}_n$ term accounts for the stretching of the radial line. The $\boldsymbol{\omega}_n \times \mathbf{l}_n$ term describes the drag-producing normal velocity. The angular velocity of the radial line is $\boldsymbol{\omega}_n$, which is given by

$$\begin{aligned} \mathbf{l}_n \times \mathbf{v}_s &= \mathbf{l}_n \times (\dot{\mathbf{l}}_n + \boldsymbol{\omega}_n \times \mathbf{l}_n) \\ \Rightarrow \boldsymbol{\omega}_n &= \frac{\mathbf{l}_n \times \mathbf{v}_s}{\|\mathbf{l}_n\|_2^2}. \end{aligned} \quad (\text{D.2})$$

Using (C.1), the aerodynamic drag force on the element dx is given by

$$d\mathbf{F}_n = 4\pi\eta\epsilon(\boldsymbol{\omega}_n \times \mathbf{x})dx$$

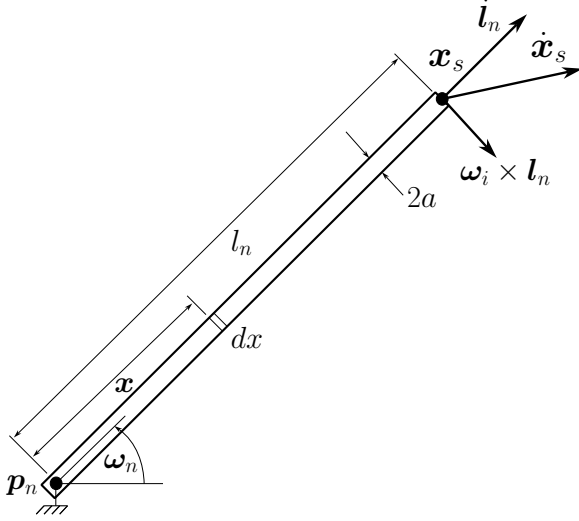


Figure D.1: Dynamics of a radial web fibre.

for a cylinder vibrating normal to its length. Taking moments about p_n gives

$$\begin{aligned} dM_n &= \mathbf{x} \times d\mathbf{F}_n \\ &= 4\pi\eta\epsilon\mathbf{x} \times (\boldsymbol{\omega}_n \times \mathbf{x})dx \\ &= 4\pi\eta\epsilon x^2 \boldsymbol{\omega}_n dx. \end{aligned} \quad (\text{D.3})$$

While the Reynolds number varies along the length of the pendulum, one might approximate this influence using a fixed Reynolds number, such as that corresponding to $0.7 \times$ tip velocity in (C.1). This assumption is based on the observation that the total moment is dominated by the drag force contribution closer to the spider. Under this assumption we obtain

$$M_n|_{Re \text{ Const}} = \int_0^{l_n} \frac{dM_n}{dx} dx = \frac{4}{3}\pi\eta\epsilon l_n^3 \boldsymbol{\omega}_n. \quad (\text{D.4})$$

If we allow the Reynolds number to vary as a function of x in (C.1), there holds

$$\begin{aligned} M_n &= \int_0^{l_n} \frac{dM_n}{dx} dx = 4\pi\eta \int_0^{l_n} \frac{x^2 dx}{1 - \gamma - \log\left(\frac{2ax\omega_n}{8\nu}\right)} \boldsymbol{\omega}_n \\ &= \boldsymbol{\omega}_n \frac{256\pi\eta\nu^3 e^{\left(\frac{3}{2} - 3\gamma\right)} Ei\left(6 \log(2) - 3 \log\left(\frac{l_n a \omega_n}{\nu}\right) + \frac{3}{2} - 3\gamma\right)}{\omega_n^2 a^3} \end{aligned} \quad (\text{D.5})$$

in which $Ei(\cdot)$ is the exponential integral²³. Figure D.2 shows the difference between (D.4) and (D.5) with Re fixed at .7 time the high-end value, as functions of the radial length $\|\mathbf{l}_n\|_2$ and the angular velocity $\boldsymbol{\omega}_n$. There is no significant difference between (D.4) and (D.5) with a fixed Reynolds number.

We can now conclude that the drag force acting on the spider due to the n^{th} radial line satisfies $\mathbf{l}_n \times \mathbf{F}_n^r = M_n$. Thus

$$\mathbf{l}_n \times (\mathbf{l}_n \times \mathbf{F}_n^r) = \mathbf{l}_n \times M_n, \quad (\text{D.6})$$

giving

$$\mathbf{F}_n^r = \frac{-1}{\|\mathbf{l}_n\|_2^2} (\mathbf{l}_n \times M_n) \quad (\text{D.7})$$

which is the force on the spider due to the aerodynamic drag on the n^{th} radial line. The cumulative effect across the n radial lines can be found by summation.

At an intuitive level one would expect the drag on the radial lines to be small, but not insignificant. First, much of the radial line dynamic change is in non-drag-producing elongation. Second, the angular velocities of the radial lines are likely to be small, so that the normal drag-producing velocity components are also small.

E. Drag on the capture lines

Figure E.1 shows the n^{th} radial line together with those adjacent to it; all three are connected by parts of the capture fibres. There are N radial threads and M equispaced capture threads; see also Figure 1. The m^{th} capture line running from radial line $n-1$ to n is vector \mathbf{c}_{m-1} , while the m^{th} capture line running from radial line n to $n+1$ is vector \mathbf{c}_{m+1} . Since the velocity of the spider is $\dot{\mathbf{x}}_s$, the velocity of the j^{th} capture line is given by proportion

$$\mathbf{v}_m = \frac{M+1-m}{M+1} \dot{\mathbf{x}}_s; \quad 1 \leq m \leq M. \quad (\text{E.1})$$

The drag-producing components of \mathbf{v}_m orthogonal to \mathbf{c}_{m-1} and \mathbf{c}_{m+1} are given by

$$\mathbf{v}_{m-1}^\perp = \mathbf{v}_m - \frac{\mathbf{v}_m \cdot \mathbf{c}_{m-1}}{\|\mathbf{c}_{m-1}\|_2^2} \mathbf{c}_{m-1} \quad (\text{E.2})$$

$$\mathbf{v}_{m+1}^\perp = \mathbf{v}_m - \frac{\mathbf{v}_m \cdot \mathbf{c}_{m+1}}{\|\mathbf{c}_{m+1}\|_2^2} \mathbf{c}_{m+1}. \quad (\text{E.3})$$

These velocity components will produce aerodynamic drag forces

$$\mathbf{F}_{m-1} = 4\pi\eta\epsilon c_{m-1} \mathbf{v}_{m-1}^\perp, \quad (\text{E.4})$$

$$\mathbf{F}_{m+1} = 4\pi\eta\epsilon c_{m+1} \mathbf{v}_{m+1}^\perp, \quad (\text{E.5})$$

that act on the web sections c_{m-1} and c_{m+1} using (C.1). Assuming these forces are shared evenly between neighbouring radial threads, \mathbf{F}_{m-1} and \mathbf{F}_{m+1} will produce force

$$\mathbf{f}_m^n = \frac{\mathbf{F}_{m-1} + \mathbf{F}_{m+1}}{2} = 2\pi\eta\epsilon (c_{m-1} \mathbf{v}_{m-1}^\perp + c_{m+1} \mathbf{v}_{m+1}^\perp),$$

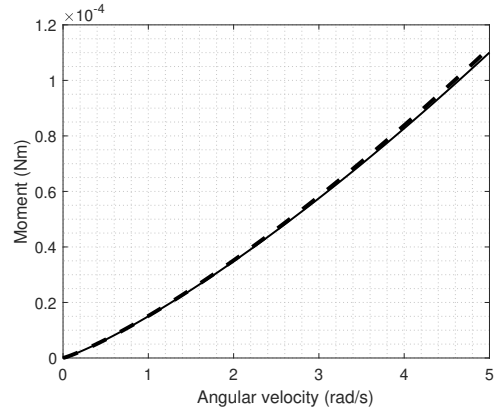
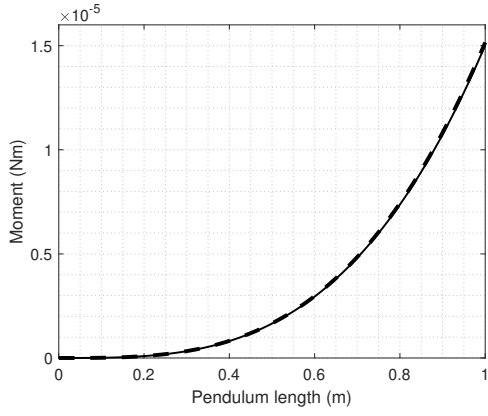


Figure D.2: Aerodynamic drag on the radial lines. The solid line is generated by (D.4) with the Reynolds number fixed at 0.7 times the tip speed. The dashed line comes from (D.5). The left-hand plot shows the generated moment as a function of pendulum length at $\|\omega_n\|_2 = 1$. The right-hand plot shows the generated moment as a function of the pendulum angular velocity at $\|l_n\|_2 = 1$.

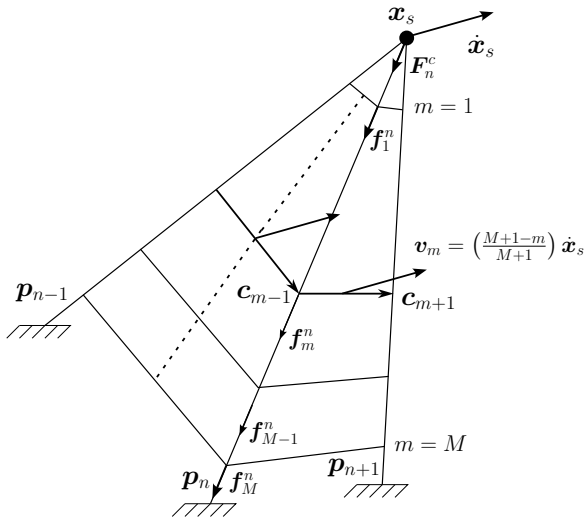


Figure E.1: Drag forces on the capture lines. The n^{th} radial line goes from p_n to x_s ; those adjacent to it are also shown. The velocity of the spider is given by \dot{x}_s . The m^{th} equispaced capture line has velocity $v_m = \frac{M+1-m}{M+1} \dot{x}_s$; M is the total number of capture line rings.

$$(E.6)$$

that acts on the n^{th} radial line.

The cumulative action of f_m^n for $1 \leq m \leq M$ on the n^{th} radial line is illustrated in Figure E.2. If the n^{th} radial line is

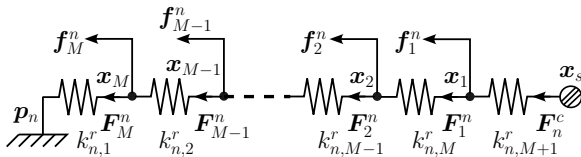


Figure E.2: The capture line forces acting on the n^{th} radial line and spider.

divided into $M + 1$ partitions, the stiffness of each partition

is $(M + 1)k_n^r$; see (A.4). The $m + 1$ incremental distances along the n^{th} radial line sum to give

$$x_s = \frac{-1}{(M + 1)k_n^r} \left(F_n^c + \sum_{m=1}^M F_m^n \right). \quad (E.7)$$

Referring to Figure E.2, and working from right to left, it can be seen that

$$\begin{aligned} F_1^n &= F_n^c - f_1^n \\ F_2^n &= F_n^c - f_1^n - f_2^n \\ &\vdots \\ F_{M-1}^n &= F_n^c - f_1^n - \dots - f_{M-2}^n - f_{M-1}^n \\ F_M^n &= F_n^c - f_1^n - \dots - f_{M-2}^n - f_{M-1}^n - f_M^n \end{aligned} \quad (E.8)$$

with the general term given by

$$F_m^n = F_n^c - \sum_{j=1}^m f_j^n. \quad (E.9)$$

Substituted into (E.7) gives

$$\mathbf{x}_s = \frac{-1}{k_n^r} \left\{ \mathbf{F}_n^c - \sum_{m=1}^M \frac{M+1-m}{M+1} \mathbf{f}_m^n \right\}. \quad (\text{E.10})$$

The total force on the spider is due to both the stiffness of the n^{th} radial line and the accumulated drag forces. The aerodynamic drag force component is:

$$\mathbf{F}_n^c = \sum_{m=1}^M \frac{M+1-m}{M+1} \mathbf{f}_m^n. \quad (\text{E.11})$$

In order to find the cumulative effect of the capture line drag forces, it is necessary to sum these forces for every radial line. The capture lines nearest to the spider will be shortest, but will be subject to the highest normal velocity, as well as having the largest $\frac{M+1-m}{M+1}$ weighting in (E.11). If the web is constructed with a dense mesh of capture lines, their cumulative drag effect is likely to be the dominant aerodynamic influence.

F. Flow interference

Conditions under which cylinders can be treated as isolated and independent has been studied experimentally^{24,25}, but this work is for Reynolds numbers which are orders of magnitude greater than applies here for oscillating web fibres. In our case the Reynolds number range is $Re < 1$, but the flow's Keulegan–Carpenter number can be $K_c \sim 10^4$. We showed in Appendix C that the Keulegan–Carpenter number is the ratio of the convective acceleration to the unsteady term in the Navier-Stokes equations (B.1). In the same way the ratio of the convective acceleration to the unsteady term in the viscous term is the Reynolds number. This means that

$$Re \sim K_c \left(\frac{a}{\delta} \right)^2,$$

and a small $\frac{a}{\delta}$, combined with small Keulegan–Carpenter number, enforce a small Reynolds number.

Stokes was able to solve the interacting cylinder problem for low Reynolds numbers by neglecting the nonlinear convective acceleration term in (B.1)⁸. Unfortunately, Stokes theory cannot be relied on here, because it only treats very-low amplitude conditions. To address this problem, at least in part, one can solve (B.1) with the convective acceleration term replaced with the Oseen approximation $(v_0 \cdot \nabla)v$ in which v_0 is the mean flow velocity; this substitution leaves (B.1) linear and still amenable to analytic solution¹⁸. The Oseen approximation bridges the gap between viscous flow solutions and a full Navier-Stokes solution.

If an infinite cylinder oscillates at frequency ω and peak amplitude v_0 , then the disturbed air velocity at perpendicular distance r from the cylinder is given by

$$v(r, \omega) = v_0 \frac{K_1(\lambda r)}{K_1(\lambda a)} e^{i\omega t} \quad \text{with } \lambda = \frac{1-i}{\delta} \sqrt{1 - \frac{iv_0\delta}{2\nu}}, \quad (\text{F.1})$$

in which a is the radius of the cylinder, δ is the boundary layer thickness, and $K_1(\cdot)$ is a modified Bessel function of the second kind and first order. At low frequencies $a \ll \delta$,

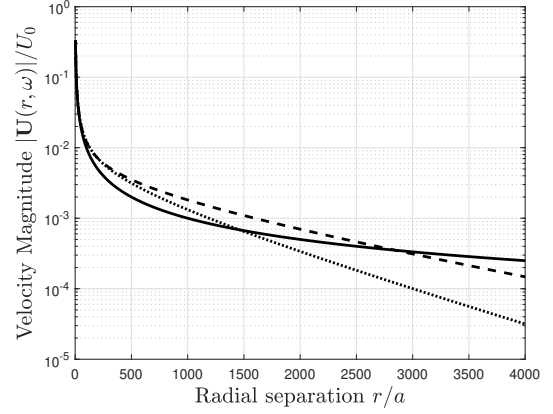


Figure F.1: Decay of the flow velocity in the neighbourhood of an oscillating cylinder. The dotted and dashed lines are for (F.1) with $\omega = 100$ rad/s and $\omega = 500$ rad/s respectively, while the solid line is for (F.2).

viscous diffusion can track the web oscillations leading to a quasi-steady-state solution. Under these condition (F.1) can be replaced with the quasi-steady-state approximation

$$v(r) \approx \frac{v_0 a}{r} \left(1 + \left(\frac{v_0 a}{4\nu} \right)^2 \log(r/a) + \text{HOTs} \right) \quad (\text{F.2})$$

which is now independent of frequency; the bracketed term is the Oseen correction.

Figure F.1 shows the decay of $|v(r)|/v_0$ at two biologically-relevant frequencies and at steady-state, as a function of r/a . In the case of a web with uniformly spaced radial lines, the maximum flow velocity due to a neighbouring cylinder is $\approx 0.001 U_0$ at 4000 web-fibre radii (or 1.5 spider diameters). Similarly interferences occur at the intersections between the radial and capture lines of the web, which are insignificant except within distances of 1 mm or less from an intersection. We will therefore ignore the effect of aerodynamic interference on the web motion, since it will be less than the uncertainty in the values of line diameters and spider drag coefficient.

If the overall resistance of the web to a relative flow velocity U_∞ incident on each web fibre is ΔU_∞ . As an example, consider the case of $N = 10$ radial lines and $M = 10$ capture lines with diameter $d = 1 \mu\text{m}$, and a web diameter of $D = 0.05$ m. In combination, their cross sectional area is given by $A \approx NDd/2 + \sum_{i=1}^M \frac{i}{M+1} \pi Dd = 1.04e^{-6} \text{m}^2$. The web's porosity is thus $\beta = (1 - \text{thread area} / \text{web area}) = 0.9995$. A relationship between the velocity reduction factor and porosity is $a = \Delta U_\infty / U_\infty \approx (1 - \beta^2) / (5 - \beta^2) = 2.64e^{-4}$ ²⁶. From this we concluded that the blocking influence of the web can also be neglected.

G. Further test results

In Test 3 the capture web density is increased as compared to Test 1; the dynamic responses are shown in Figure G.1. Despite a significant increase in the number of radial threads, the force distribution across the web is relatively unaffected as compared to Test 1. This highlights the structural insignificance of the capture threads. For the same reason, the web's

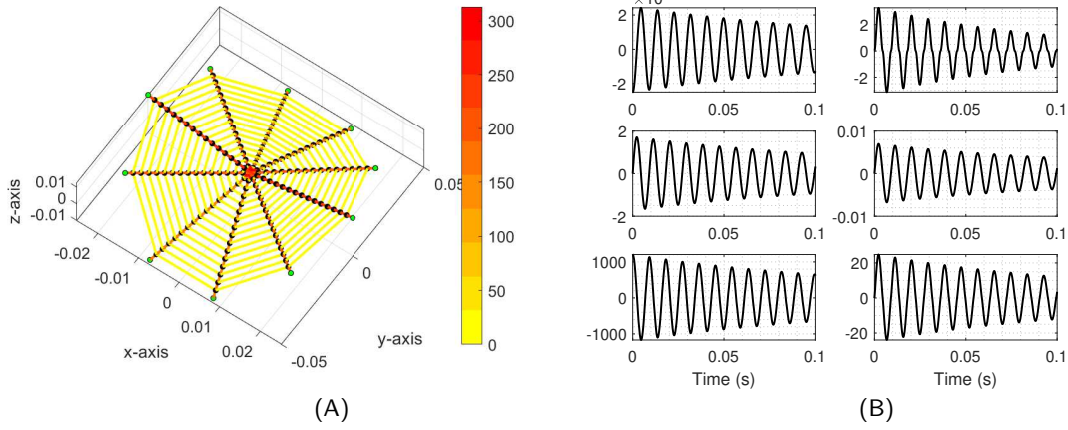


Figure G.1: Test 3: The (A) figure shows the loaded web immediately prior to the release of the tension line; the force colour bar is in μN . The left-hand side of the (B) figure shows, from the top, the spider's position (m), velocity (ms^{-1}) and acceleration responses (ms^{-2}). The right-hand part of the (B) figure shows, from the top, the spider's spherical damping force, the damping force due to the radial threads and the damping force due to the capture threads; all are in μN .

resonant frequencies are relatively unaffected by the increase in capture thread density (there is only a small reduction). The peak spider- and radial-fibre-related damping force are relatively unchanged. In contrast, the peak damping force due to the capture lines increases by a factor of ≈ 2.5 .

In the Test 4, a larger web with a thinly-populated capture mesh is studied—the dynamic responses in this case are shown in Figure G.2. As one would now expect, when comparing Tests 4 and 6, the change in the number of capture lines in having a relatively minor impact of the structural features of the web including the loaded force distribution and the undamped natural frequencies; the influence of web damping does manifest in the damped natural frequency however. Despite the thin capture web, the aerodynamic damping is having a significant influence on the web response. This was not the case in Test 1, since the smaller web is relatively stiff structurally in that case. As compared with Test 6, the total damping force is reduced as expected. Referring to Table 1, it is observed that the peak spider and radial-fibre-related damping forces increase slightly due to small velocity increases. However, the peak value of the capture-fibre-related damping force is significantly reduced from $202 \mu\text{N}$ to $83.8 \mu\text{N}$.

Plots reminiscent of Figure 7 show that in all the tests conducted, the real strains in every anchor line operate below 20% and so are expected to remain below the web-fibre's elastic limit throughout the test oscillatory transients. Furthermore, since the minimum strain is positive, these fibres remain in tension throughout the oscillatory transients.

H. Neglect of the history and added-mass terms

Following¹³, we use a simple calculation to illustrate the relative importance of the velocity, acceleration and history terms in (B.4), and thus why the history and added-mass terms can be neglected. Suppose that the displacement, velocity, and acceleration of the sphere, respectively, are given by

$$d = A_0 \cos \omega t \quad (\text{H.1})$$

$$v = -A_0 \omega \sin \omega t \quad (\text{H.2})$$

$$a = -A_0 \omega^2 \cos \omega t. \quad (\text{H.3})$$

This gives

$$F_s = \frac{1}{2} C_D \rho \pi r_s^2 \omega^2 A_0^2 |\sin \omega t| \sin \omega t - C_A \left(\frac{4}{3} r_s^3 \rho \right) A_0 \omega^2 \cos \omega t + C_H r_s^2 A_0 \omega^{\frac{3}{2}} \pi \sqrt{2\nu\rho} \left(C \left(\sqrt{\frac{2t\omega}{\pi}} \right) \cos \omega t + S \left(\sqrt{\frac{2t\omega}{\pi}} \right) \sin \omega t \right), \quad (\text{H.4})$$

where $C_D = 0.4$, $C_A = 0.5$, and $C_H = 6$, with $A_0 = 0.05$, $\omega = 250 \text{ rad/s}$ and $r_s = 0.65 \times 1.0^{-3} \text{ m}$ is the radius of the spider. We use the fact that

$$\int_0^t \frac{\cos \omega \tau}{\sqrt{t-\tau}} d\tau = \sqrt{2\pi\omega}^{\frac{3}{2}} \left(C \left(\sqrt{\frac{2t\omega}{\pi}} \right) \cos \omega t + S \left(\sqrt{\frac{2t\omega}{\pi}} \right) \sin \omega t \right),$$

where $C(\cdot)$ and $S(\cdot)$ are the Fresnel cosine and sine integrals²³. The first term on the right-hand side of (H.4) is the velocity term, the second is the added-mass term, while the third is the history term.

The three force terms in (H.4) are shown in Figure H.1 for the appropriate spider-web-related data. For the data associated with this problem, Figure H.1 is used to justify the neglect of the added-mass and history terms.

I. Parameters

The basic material and geometric characteristics of the spider and web are summarised in Table ??.

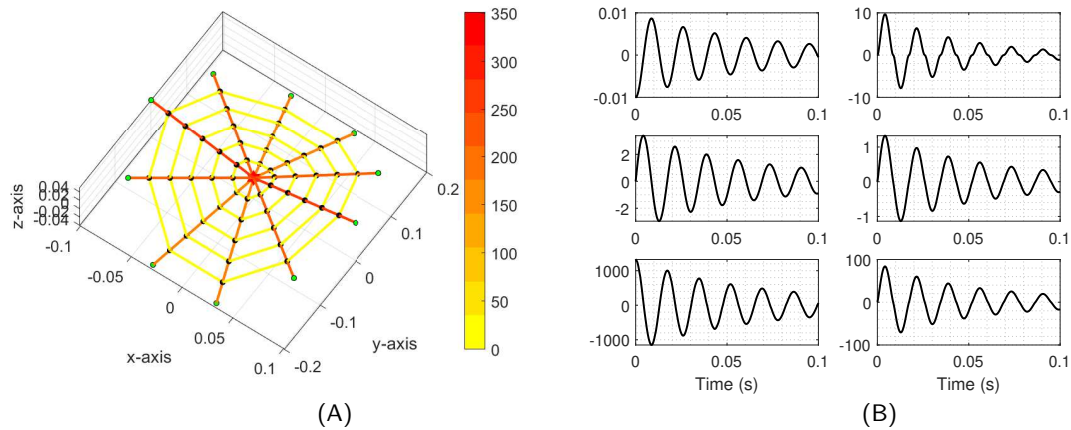


Figure G.2: Test 4: The (A) figure shows the loaded web immediately prior to the release of the tension line; the force colour bar is in μN . The left-hand side of the (B) figure shows, from the top, the spider's position (m), velocity (ms^{-1}) and acceleration responses (ms^{-2}). The right-hand part of the (B) figure shows, from the top, the spider's spherical damping force, the damping force due to the radial threads and the damping force due to the capture threads; all are in μN .

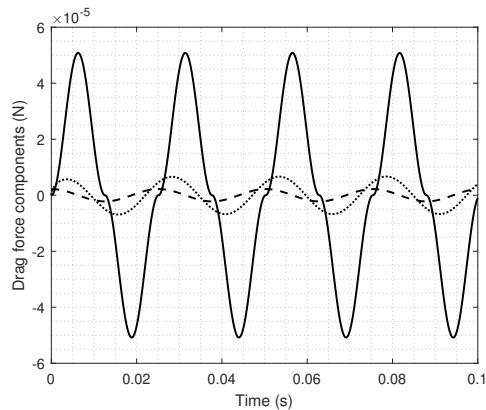


Figure H.1: Three drag force components acting on a sphere. The velocity component is solid, the acceleration component is dashed, while the history component is dotted.

References

1. R. Connelly. Rigidity and energy. *Inventiones Mathematicae*, 66:11 to 33, 1982.
2. E. D. Sanders, A. S. Ramos, and G. H. Paulino. Topology optimization of tension-only cable nets under finite deformations. *Structural and Multidisciplinary Optimization*, 62:559–579, 2020.
3. F. K. Ko and J. Jovicic. Modeling of mechanical properties and structural design of spider web. *Biomacromolecules*, 5(3):780–785, 2004.
4. M.S. Alam, M.A. Wahab, and C.H. Jenkins. Mechanics in naturally compliant structures. *Mechanics of Materials*, 39:145–160, 2007.
5. S. Boyd and L. Vandenberghe. *Convex optimisation*. Cambridge University Press, Cambridge, 2004.
6. E. Wirth and F. G. Barth. Forces in the spider orb web. *J Comp Physiol A*, 171:359 to 371, 1992.
7. Y. Aoyanagi and K. Okumura. Simple model for the mechanics of spider webs. *Phys Rev Letters*, 104:038102, 2010.
8. G. G. Stokes. On the effect of the internal friction of fluids on the motion of pendulums. *Camb. Phil. Soc.*, 9:8 to 106, 1851.
9. J. Jäger, B. Schuderer, and W. Schoepe. Translational oscillations of a microsphere in superfluid helium. *Physica B*, 210:201 to 208, 1995.
10. A. B. Basset. On the motion of a sphere in a viscous liquid. *Philosophical Transactions of the Royal Society of London (A)*, 179:43 to 63, 1887.
11. J. V. Boussinesq. Sur la résistance qu'oppose un liquide . . . au mouvement varié d'une sphere solide . . . et produits soient négligeables. *C.R. Acad. Sci. Paris*, 100, 1885.
12. C. W. Oseen. *Hydrodynamik*. Akademische Verlagsgesellschaft, Leipzig, 1927.
13. F. Odar. Forces on a sphere accelerating in a viscous fluid. *Journal of Fluid Mechanics*, 18(2):302 to 314, 1964.

14. J. R. Morison, M. P. O'Brien, J. W. Johnson, and S. A. Schaf. The force exerted by surface wave on piles. *Petroleum Trans.*, 189:149 to 157, 1950.
15. H. Schlichting. *Boundary Layer Theory*. McGraw-Hill, New York, 1955.
16. F. A. Morrison. Data correlation for drag coefficient for sphere. Technical report, Michigan Technological University, Houghton, MI, 2016.
17. H. Lamb. On the uniform motion of a sphere through a viscous fluid. *The London, Edinburgh, and Dublin Philosophical Magazine and Journal of Science*, 21(121):112 to 121, 1911.
18. C. W. Oseen. Über die Stokes'sche formel und über eine verwandte aufgabe in der hydrodynamik. *Arkiv för matematik, astronomi och fysik*, 6(29), 1911.
19. S. Kaplun. Low Reynolds number flow past a circular cylinder. *Journal of Mathematics and Mechanics*, 6(5):595 to 603, 1957.
20. R. E. Williams and R. G. Hussey. Oscillating cylinders and the Stokes' paradox. *Physics of fluids*, 15(12):2083 to 2088, 1972.
21. J. R. Clift, J. Grace, and M.E. Weber. *Bubbles, Drops and Particles*. Dover, 1978.
22. P.W. Bearman, J.M.R. Graham, and E.D. Obasaju. A model equation for the transverse forces on cylinders in oscillatory flows. *Applied Ocean Research*, 6:166 to 172, 1984.
23. M. Abramowitz and I. Stegun. *Handbook of Mathematical Functions*. Dover Publications Inc., New York, 1965.
24. M.M. Zdravkovich and D.L. Pridden. Interference between two circular cylinders; series of unexpected discontinuities. *Journal of Industrial Aerodynamics*, 2:255 to 270, 1977.
25. M. M. Zdravkovich. The effect of interference between circular cylinders in cross flow. *Journal of Fluids and Structures*, 1:239–261, 1987.
26. G. I. Taylor and R. M. Davies. The aerodynamics of porous sheets. Technical report, Aeronautical Res. Coun. 2237, 1944.